

DEALing with Image Reconstruction: Deep Attentive Least Squares

Mehrsa Pourya[†], Erich Kobler[‡], Michael Unser[†], Sebastian Neumayer^{* *}

[†] Biomedical Imaging Group, EPFL Lausanne, Switzerland

[‡] Institute for Machine Learning, LIT AI lab, Institute for Virtual Morphology, Johannes Kepler University Linz

^{*} Faculty of Mathematics, TU Chemnitz, Germany

Abstract

State-of-the-art image reconstruction often relies on complex, highly parameterized deep architectures. We propose an alternative: a data-driven reconstruction method inspired by the classic Tikhonov regularization. Our approach iteratively refines intermediate reconstructions by solving a sequence of quadratic problems. These updates have two key components: (i) learned filters to extract salient image features, and (ii) an attention mechanism that locally adjusts the penalty of filter responses. Our method achieves performance on par with leading plug-and-play and learned regularizer approaches while offering interpretability, robustness, and convergent behavior. In effect, we bridge traditional regularization and deep learning with a principled reconstruction approach.

1. Introduction

Image reconstruction plays a fundamental role in computational imaging and computer vision [30, 50]. The task is to recover an unknown image of interest $\mathbf{x} \in \mathbb{R}^d$ from noisy measurements $\mathbf{y} \in \mathbb{R}^M$. Their relation is often modeled as $\mathbf{y} = \mathbf{H}\mathbf{x}$, where the forward operator $\mathbf{H} \in \mathbb{R}^{M \times d}$ encodes the acquisition process. If \mathbf{H} is ill-conditioned, one resorts to regularized reconstruction

$$\hat{\mathbf{x}} \in \arg \min_{\mathbf{x} \in \mathbb{R}^d} \|\mathbf{H}\mathbf{x} - \mathbf{y}\|_2^2 + \lambda \mathcal{R}(\mathbf{x}). \quad (1)$$

The data-fidelity $\|\mathbf{H}\mathbf{x} - \mathbf{y}\|_2^2$ controls the consistency of the reconstruction with the measurements. The regularizer $\mathcal{R}: \mathbb{R}^d \rightarrow \mathbb{R}_{\geq 0}$ encodes prior information about the solution and is also intended to make the problem well-posed. Both terms are balanced by the hyperparameter $\lambda \in \mathbb{R}_{\geq 0}$. Throughout this paper, \mathbf{x} is the vectorized version of a (color or grayscale) image with shape $N_{\text{in}} \times H \times W$.

From classic signal processing to the advent of deep learning, a significant body of research focuses on the design of the regularizer \mathcal{R} . In the context of data-driven methods, two primary approaches emerged: (i) the explicit modeling of \mathcal{R} , and (ii) the

modeling of operators associated with \mathcal{R} , such as its proximal operator, which is required in Plug-and-Play (PnP) reconstruction algorithms [46]. Following the explicit approach, the starting point for this work is the fields-of-experts model [40], which reads

$$\mathcal{R}_{\mathbf{m}}: \mathbf{x} \mapsto \sum_{c=1}^{N_C} \langle \mathbf{m}_c, \psi_c(\mathbf{W}_c \mathbf{x}) \rangle. \quad (2)$$

Here, each $\mathbf{W}_c \in \mathbb{R}^{HW \times d}$ convolves \mathbf{x} with a filter template $w_c \in \mathbb{R}^{N_{\text{in}} \times k_s \times k_s}$. Then, the nonnegative potentials $\psi_c \in \mathcal{C}(\mathbb{R})$ are applied entry-wise to the $\mathbf{W}_c \mathbf{x}$. Finally, the weights $\mathbf{m}_c \in [\epsilon_M, 1]^{HW}$ with $\epsilon_M > 0$ determine the (spatially varying) contribution of $\psi(\mathbf{W}_c \mathbf{x})$ to the regularizer. In principle, every component of (2) can be learned. Most implementations so far have used constant weights $\mathbf{m}_c = \mathbf{1}$ in (2). Recent works differ in the parameterization of ψ_c and \mathbf{W}_c for the learning process [6, 12, 49] or incorporate non-linear feature transforms [27, 20]. While learning \mathbf{W}_c and ψ_c is extensively studied, little research is performed regarding the local weights \mathbf{m}_c .

Employing spatially varying \mathbf{m}_c in (2) is referred to as anisotropic regularization. For instance, $\mathbf{m}_c = \mathbf{M}(\mathbf{y})$ can be derived from the data \mathbf{y} using heuristics [5, 13] or a neural network [21, 23]. When \mathbf{M} extracts features from an estimated reconstruction, as proposed by Neumayer and Altekrüger [31], it is natural to consider refining \mathbf{m}_c iteratively. Specifically, the reconstruction from (1) can be fed back into \mathbf{M} to obtain an *improved* \mathbf{m}_c for (2). This leads to the attentive reconstruction process

$$\mathbf{x}_{k+1} \in \arg \min_{\mathbf{x} \in \mathbb{R}^d} \|\mathbf{H}\mathbf{x} - \mathbf{y}\|_2^2 + \lambda \mathcal{R}_{\mathbf{M}(\mathbf{x}_k)}(\mathbf{x}), \quad (3)$$

studied by Pourya et al. [35] for $\psi_c = |\cdot|$. We note that their scheme is computationally demanding since each update involves a least absolute shrinkage and selection operator (LASSO)-type problem.

Contribution The updates (3) are the starting point of our investigation. Our contributions are as follows.

- We simplify the updates (3) by choosing $\psi_c(\cdot) = (\cdot)^2$ for the $\mathcal{R}_{\mathbf{M}(\mathbf{x}_k)}$ from (2). Then, each update

*mehrsa.pourya@epfl.ch, erich.kobler@jku.at, michael.unser@epfl.ch, sebastian.neumayer@mathematik.tu-chemnitz.de

amounts to solving a linear equation, which we handle efficiently through the conjugate gradient method.

- We learn the components of $\mathcal{R}_{\mathbf{M}(\mathbf{x}_k)}(\mathbf{x})$, namely the filters $\{\mathbf{W}_c\}_{c=1}^{N_c}$ and the attention mechanism \mathbf{M} , based on a denoising task in such a way that the iterations (3) converge. Then, any fixed point of (3) is a consistent reconstruction. Given a linear inverse problem with forward \mathbf{H} , we then apply our learned model with only two remaining hyperparameters: (i) the noise level and (ii) the regularization strength λ .
- On the theoretical side, we establish the uniqueness of each update in (3), the existence of a fixed point, a condition for the convergence of (3), and a stability result for the resulting reconstruction operator.
- In our experimental evaluation, we achieve results on par with state-of-the-art approaches for various inverse problems.
- We underline the interpretability, convergence, and robustness of our method. We provide illustrative examples to visualize the learned attention mechanism.

2. Related Literature

Learned Regularization Classical regularizers for (1) leverage sparsity in various domains, such as image gradients [41] or wavelets [29]. The parametric model (2) introduced by Roth and Black [40] has since spurred extensive research. Key areas of investigation include learning paradigms [6, 10], parametrization strategies [49], and intrinsic properties like convexity [11, 12]. More complex architectures build upon strategies such as autoencoders [27], algorithm unrolling [20], adversarial training [28, 37], and energy modeling [48].

In parallel, implicit regularization methods were developed. Here, of-the-shelf denoisers are incorporated into iterative reconstruction algorithms by, for instance, replacing proximal operators [46, 54] or drawing inspiration from adaptive Laplacians [39]. If the denoiser is non-expansive or homogeneous, which is hard to ensure for learned ones [38, 14], this leads to a convergent scheme. Recently, weaker conditions have been proposed by Pesquet et al. [34], Hurault et al. [17].

Spatial Adaptivity An overview of spatially adaptive regularizers with the form (2) is given in Pragliola et al. [36]. The authors Hintermüller et al. [15], Van Chung et al. [45], Kofler et al. [21] focus on the total variation regularizer [41] as a special case, using either heuristics or deep learning to compute

the weights \mathbf{m}_c . More general instances are considered by Lefkimmiatis and Koshelev [23], Neumayer et al. [32], Neumayer and Altekruiger [31]. The first work deploys non-smooth potentials ψ_c and majorization minimization to solve the nonsmooth problem (1). Similar to (3), this leads to a series of quadratic problems. The latter works deploy differentiable ψ_c and solve (1) with accelerated gradient descent. All approaches have in common that they update the weights \mathbf{m}_c only once. In particular, they do not refine \mathbf{m}_c and the reconstruction iteratively as in (3).

Iterative Refinement Lenzen et al. [24], Lenzen and Berger [25] propose to iteratively refine the weights \mathbf{m}_c for total variation. They update the \mathbf{m}_c using some heuristic. For the more general model (2) with $\psi_c = |\cdot|$, a refinement based on neural networks was considered by Pourya et al. [35]. Their \mathbf{M} has a simple architecture comparable to ours. Outside of this setting, iterative refinement can be found, for example, in Saharia et al. [42] for superresolution and in Darestani et al. [8] for MRI.

Nonlocal Laplacians Quadratic potentials ψ_c lead to an optimality condition for (3) induced by a symmetric positive semi-definite matrix. A different approach to getting such updates is (iterative) filtering with carefully designed graph Laplacians [33]. Recently, this idea was incorporated into deep architectures for image denoising [51, 44] and scene flow [43].

3. Methodology

We specify the regularizer (2) using quadratic potentials as

$$\mathcal{R}_{\mathbf{m}}(\mathbf{x}) = \sum_{c=1}^{N_c} \langle \mathbf{m}_c^2, (\mathbf{W}_c \mathbf{x})^2 \rangle = \|\mathbf{M}\mathbf{W}\mathbf{x}\|_2^2 \quad (4)$$

with the shorthands $\mathbf{W} = [\mathbf{W}_1^\top \dots \mathbf{W}_{N_c}^\top]^\top$ and $\mathbf{M} = \text{Diag}(\text{Diag}(\mathbf{m}_1), \dots, \text{Diag}(\mathbf{m}_{N_c}))$, where Diag returns a diagonal matrix whose entries are the input vector. This leads to the quadratic reconstruction problem

$$\hat{\mathbf{x}} \in \arg \min_{\mathbf{x} \in \mathbb{R}^d} \|\mathbf{H}\mathbf{x} - \mathbf{y}\|_2^2 + \lambda \|\mathbf{M}\mathbf{W}\mathbf{x}\|_2^2. \quad (5)$$

Now, the question arises about the proper choice of \mathbf{M} and \mathbf{W} . Regarding a filter-based interpretation, the \mathbf{W} should be independent of \mathbf{y} . \mathbf{M} modulates the response $\mathbf{W}\mathbf{x}$ at each location. Ideally, this modulation should depend on the structure of the (unknown) $\hat{\mathbf{x}}$. With abuse of notation, we introduce $\mathbf{M}: \mathbb{R}^d \rightarrow [\epsilon_M, 1]^{N_c H W}$, which leads to our attentive

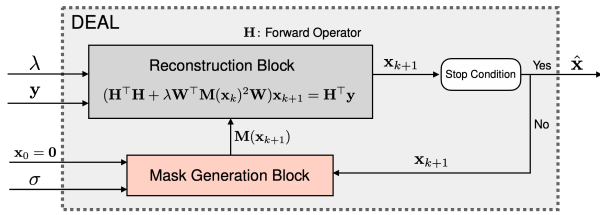


Figure 1: DEAL generates a sequence of reconstructions \mathbf{x}_k via (6) from the inputs \mathbf{y} and \mathbf{H} , initialization $\mathbf{x}_0 = \mathbf{0}$, and hyper-parameters σ and λ . When the stop condition is met, it returns $\hat{\mathbf{x}}$.

refinement scheme

$$\mathbf{x}_{k+1} \in \mathcal{T}(\mathbf{x}_k, \mathbf{y}) \quad \text{with} \quad \mathbf{x}_0 = \mathbf{0} \in \mathbb{R}^d, \quad (6)$$

$$\mathcal{T}(\mathbf{z}, \mathbf{y}) = \arg \min_{\mathbf{x} \in \mathbb{R}^d} \|\mathbf{H}\mathbf{x} - \mathbf{y}\|_2^2 + \lambda \|\mathbf{M}(\mathbf{z})\mathbf{W}\mathbf{x}\|_2^2. \quad (7)$$

The process (6) can be interpreted as an infinite-depth neural network. Hence, we name it deep attentive least squares (DEAL) for image reconstruction. If $\mathbf{x}_k \rightarrow \hat{\mathbf{x}}$, we get $\hat{\mathbf{x}} \in \mathcal{T}(\hat{\mathbf{x}}, \mathbf{y})$, namely that $\hat{\mathbf{x}}$ is a fixed-point of the operator (7). We restrict $k < K_{\text{out}}$ and terminate the iterations (6) when $\|\mathbf{x}_{k+1} - \mathbf{x}_k\|_2 / \|\mathbf{x}_k\|_2 \leq \epsilon_{\text{out}}$ with $\epsilon_{\text{out}} > 0$.

3.1. Architecture

Next, we specify how the DEAL iterates (6) can be cast as a deep neural network structure. Figure 1 visualizes the interplay of its essential building blocks – reconstruction and mask generation – which exchange information repeatedly.

3.1.1 Reconstruction Block

At the heart of DEAL, the reconstruction block solves the spatially-adapted optimization problem (7) for given attentive weights $\mathbf{M}(\mathbf{x}_k)$ (see Section 3.1.2). The optimality condition for problem (7) is given by the linear system

$$\mathbf{A}_k \mathbf{x}_{k+1} = \mathbf{b} \quad (8)$$

with $\mathbf{A}_k = \mathbf{H}^\top \mathbf{H} + \lambda \mathbf{W}^\top \mathbf{M}(\mathbf{x}_k)^2 \mathbf{W}$ and $\mathbf{b} = \mathbf{H}^\top \mathbf{y}$. The multi-convolution block \mathbf{W} , see Section 3.1.3, and $\lambda \in \mathbb{R}$ are learnable. To avoid scaling ambiguities, we impose $\|\mathbf{W}\|_2 = 1$ by spectral normalization. The data \mathbf{y} and the forward \mathbf{H} are problem-specific inputs that are not learnable. We solve (8) by the conjugate-gradient (CG) algorithm with \mathbf{x}_k as the initial guess. We use a batched CG with at most K_{in} steps, where each sample terminates individually if its residue satisfies $\|\mathbf{A}_k - \mathbf{b}\mathbf{x}_{k+1}\|_2^2 \leq \epsilon_{\text{in}}$ for $\epsilon_{\text{in}} > 0$.

3.1.2 Mask Generation Block

To estimate \mathbf{M} for (5) from local image structures, we use the following shallow CNN with learnable

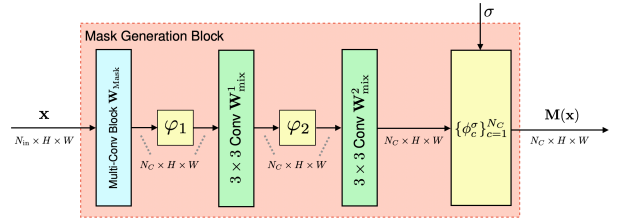


Figure 2: Architecture of the mask generation block.

nonlinearities

$$\mathbf{M}(\mathbf{x}) = (\phi^\sigma \circ \mathbf{W}_{\text{mix}}^2 \circ \phi_2 \circ \mathbf{W}_{\text{mix}}^1 \circ \phi_1 \circ \mathbf{W}_{\text{mask}})(\mathbf{x}), \quad (9)$$

see also Figure 2. This choice is inspired by anisotropic diffusion [47, 4], where \mathbf{M} is typically computed from the gradients of a smoothed image using pixel-wise non-linearities.

The first multi-conv layer \mathbf{W}_{mask} (see Section 3.1.3) in (9) extracts N_c spatial features using the same architecture as the \mathbf{W} from the reconstruction block. The two subsequent convolution layers $\mathbf{W}_{\text{mix}}^1$ and $\mathbf{W}_{\text{mix}}^2$ mix the N_c feature channels using kernels of size 3×3 and no bias. The layers are connected via learnable point-wise non-linearities ϕ_1 and ϕ_2 , for which we follow Bohra et al. [3]. Specifically, each ϕ_i is parametrized as a linear spline with N_n equally distributed knots on $[0, r]$. On (r, ∞) the splines are linearly extended and we enforce symmetry by setting $\phi(x) = \phi(-x)$ if $x < 0$. In addition, we constrain them to be increasing for $x > 0$. Removing both constraints has not led to significant performance improvements.

To guarantee the numerical stability of (8), the outputs of \mathbf{M} must remain in $(\epsilon_M, 1]$. Hence, we process each channel $c \in \{1 \dots N_c\}$ individually by

$$\phi_c^\sigma(x) = \max(\min(\phi_3(\alpha_c(\sigma)\mathbf{x}), 1), \epsilon_M), \quad (10)$$

where ϕ_3 is a symmetric linear spline as before. In contrast to the former splines, ϕ_3 must be non-increasing on $[0, \infty)$. The underlying rationale is that the $\mathbf{M}(\mathbf{x})$ should be close to 1 for small filter responses (constant image regions) and close to 0 for strong filter responses (salient edges). Following Goujon et al. [12], we enable multi-level noise training using the positive scalings

$$\alpha_c(\sigma) = \frac{e^{s_c(\sigma)}}{\sigma + 10^{-5}} \quad (11)$$

with learnable linear splines $\{s_c\}_{c=1}^{N_c}$. By design of \mathbf{M} , the first reconstruction block consists of a non-varying problem.

3.1.3 Multi-Conv Block

The Multi-Conv block advocated by Goujon et al. [11] consists of multiple convolution layers with no

non-linearities in between. It enables the efficient construction of large receptive fields. We use three convolution layers, all with kernels of size (9×9) . Thus, the effective field of view for this block is (25×25) . For inputs with N_{in} channels, the number of output channels of the convolution layers are $4N_{\text{in}}$, $8N_{\text{in}}$, and N_C , respectively. We set the group size and stride to one, and do not use a bias. In all our experiments, we use $N_C = 128$. This block appears in two places: once in $\mathbf{M}(\mathbf{x})$ as \mathbf{W}_{Mask} and second in the reconstruction block as \mathbf{W} , i.e., the convolutions in (4).

3.2. Training

We learn the parameters θ of DEAL for image denoising with additive white Gaussian noise (AWGN) of varying standard variation $\sigma_n \in [0, 50]$. The associated denoiser $D_{\theta(\sigma_n)}^{K_{\text{out}}}(\mathbf{y})$ takes the measurements \mathbf{y} and σ_n as input, and returns the solution of (6) with at most K_{out} iterations. Choosing denoising as the training task has two reasons: (i) our learned model should also work for other inverse problems (often called universality), as demonstrated by Hurault et al. [17], Goujon et al. [12]; (ii) it simplifies the computations for the reconstruction block as $\mathbf{H} = \mathbf{I}$. We provide details on initializations and hyperparameters with a short ablation study in A.

Dataset and Loss For the training dataset $\mathbf{D} = \{\mathbf{x}^m\}_{m=1}^M$, we use the images proposed in Zhang et al. [54]. The images \mathbf{x} are corrupted by AWGN as $\mathbf{y} = \mathbf{x} + \sigma_n \mathbf{n}$ and fed into DEAL, leading to a sequence of denoised images $\{\mathbf{x}_k\}_{k=1}^{K_{\text{out}}} = D_{\theta(\sigma_n)}^{K_{\text{out}}}(\mathbf{y})$. To estimate the parameters θ from the training data, we use the loss

$$\mathcal{L}(\theta) = \left\{ \mathbb{E}_{\substack{\mathbf{x} \sim \mathbf{D} \\ \sigma_n \sim \mathcal{U}([0, 50]) \\ \mathbf{n} \sim \mathcal{N}(\mathbf{0}, \mathbf{I})}} \left[\|\mathbf{x}_{K_{\text{out}}} - \mathbf{x}\|_2^2 + \right. \right. \\ \left. \left. \frac{\gamma}{N_c} \|\mathbf{M}(\mathbf{x}_{K_{\text{out}}}) - \mathbf{M}(\mathbf{x}_{K_{\text{out}}-1})\|_2^2 \right] + \gamma \text{TV}^2(\theta) \right\} \quad (12)$$

with $\gamma = 10^{-4}$. This loss consists of three parts: (i) a squared error enforcing that the output matches the clean image; (ii) a squared penalty on the weight changes for the last two updates of (6); and (iii) an accumulated second-order total variation regularization of all learnable splines. This last penalizes changes in their slopes (kinks) and thereby promotes simpler splines [3, 9]. The second term in (12) vanishes if the generated weights $\mathbf{M}(\mathbf{x}_k)$ converge. To promote convergence of (6) to a fixed point, we sample K_{out} uniformly from [15, 60] [1].

We minimize the loss (12) using Adam [18]. At each step of the optimizer, we sample 16 patches of size (128×128) randomly from \mathbf{D} . We have two training phases; first, we train the gray and color model for 70 000 and 40 000 steps respectively, using

an initial learning rate 5×10^{-4} that is reduced to 4×10^{-4} by a cosine annealing scheduler. Then, we continue training the gray and color model for 10 000 and 5000 steps, respectively, with an initial learning rate 2×10^{-4} that is reduced to 1×10^{-7} by annealing. We set $\epsilon_{\text{out}} = \epsilon_{\text{in}} = 1 \times 10^{-4}$ and the maximal of CG steps to $K_{\text{in}} = 50$. To select the best-performing model, we evaluate its performance every 1000 training step and keep the checkpoint with the best validation performance. We use the set3 and set12 datasets to validate the color and grayscale models.

Gradient Tracking We train DEAL through the deep equilibrium framework [2] in the Jacobian free mode. Specifically, we perform at most $K_{\text{out}} - 1$ iterations without gradient tracking. Then, after convergence, we perform one additional update (6) with gradient tracking. For this, it is crucial to have an efficient backward path for the reconstruction block, namely for $\partial_{\theta} \mathbf{x}_{k+1}$ as defined in (6). Since backpropagating through the CG algorithm is prohibitively memory extensive, we need another solution.

From (8), we have that

$$\mathbf{x}_{k+1} = \mathbf{y} - \lambda \mathbf{L}_k^{\top} \mathbf{L}_k \mathbf{x}_{k+1}, \quad (13)$$

where $\mathbf{L}_k = \mathbf{M}(\mathbf{x}_k) \mathbf{W}$. Using the product rule, we get

$$\partial_{\theta} \mathbf{x}_{k+1} = -\lambda \mathbf{L}_k^{\top} \mathbf{L}_k \partial_{\theta} \mathbf{x}_{k+1} - \lambda \partial_{\theta} (\mathbf{L}_k^{\top} \mathbf{L}_k) \mathbf{x}_{k+1}. \quad (14)$$

It follows

$$\mathbf{A}_k \partial_{\theta} \mathbf{x}_{k+1} = \mathbf{d}_{k+1}, \quad (15)$$

where the matrix \mathbf{A}_k is the one from (8), and only the right-hand-side changes to $\mathbf{d}_{k+1} = -\lambda \partial_{\theta} (\mathbf{L}_k^{\top} \mathbf{L}_k) \mathbf{x}_{k+1}$. We use auto-differentiation to obtain the gradient estimate \mathbf{d}_{k+1} . We then find $\partial_{\theta} \mathbf{x}_{k+1}$ by solving (15) with CG.

3.3. Inference

Once the parameters are learned, we can directly deploy DEAL to a general inverse problem by plugging the corresponding forward operator \mathbf{H} and its adjoint \mathbf{H}^{\top} into the reconstruction block. This does not affect the mask generation block. To adapt to the new task, we now only need to tune two hyperparameters: the model noise level σ and the regularization strength λ in (6). This requires a small validation set with paired measurements and ground truth images. Empirically, we observe that tuning λ is more important than changing the noise level σ . To ensure that we find a fixed point of (6), we set $K_{\text{in}} = K_{\text{out}} = 1000$, and choose the conservative stop criteria $\epsilon_{\text{in}} = 10^{-8}$ and $\epsilon_{\text{out}} = 10^{-5}$.

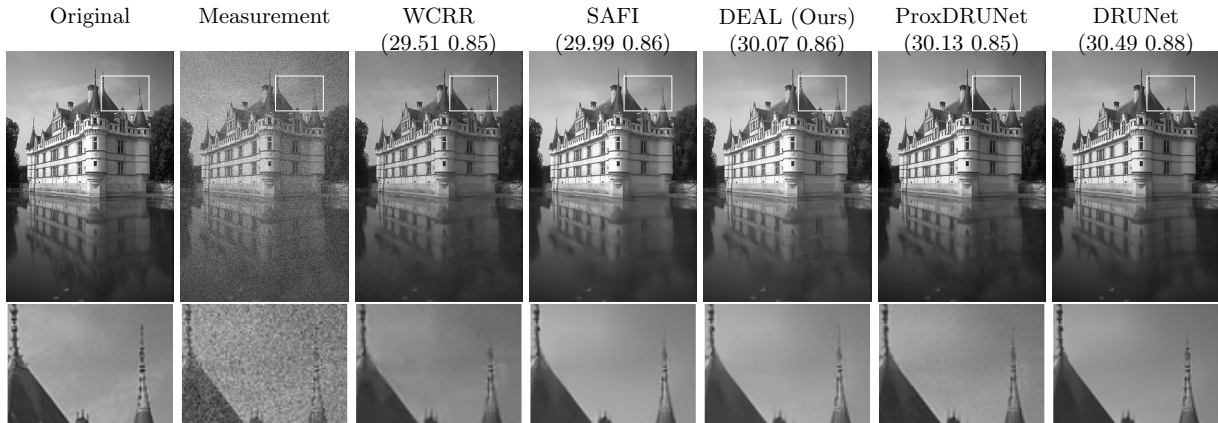


Figure 3: Denoising of the *castle* image for $\sigma = 25$. For each reconstruction (PSNR and SSIM) is provided.

4. Theoretical Results

All the proofs are provided in Appendix B. Proposition 4.1 guarantees the uniqueness of the updates (6).

Proposition 4.1. *If $\ker(\mathbf{H}) \cap \ker(\mathbf{M}(\mathbf{x}_k)\mathbf{W}) = \{\mathbf{0}\}$, then \mathbf{A}_k is positive definite and (8) has a unique solution. Moreover, if $\mathbf{M}^2(\mathbf{x}_k) \succeq \epsilon_M \text{Id}$, then $\mathbf{A}_k \succeq \mathbf{H}^\top \mathbf{H} + \epsilon_M \mathbf{W}^\top \mathbf{W}$ and uniqueness holds if $\ker(\mathbf{H}) \cap \ker(\mathbf{W}) = \{\mathbf{0}\}$.*

The next results involve an estimate of the smallest eigenvalue of \mathbf{A}_k : $\lambda_\epsilon = \lambda_{\min}(\mathbf{H}^\top \mathbf{H} + \epsilon_M \mathbf{W}^\top \mathbf{W})$.

Lemma 4.2. *Let $\mathbf{x} \in \mathbb{R}^d$. If $\ker(\mathbf{H}) \cap \ker(\mathbf{W}) = \{\mathbf{0}\}$ and $\mathbf{M}(\mathbf{x})^2 \succeq \epsilon_M \text{Id}$, then $\mathcal{T}(\mathbf{x}, \cdot): \mathbb{R}^M \rightarrow \mathbb{R}^d$ is Lipschitz continuous with constant $\|\mathbf{H}\|_2 / \lambda_\epsilon$.*

Next, we establish the existence of fixed points for $\mathcal{T}(\cdot, \mathbf{y})$.

Theorem 4.3. *Assume $\ker(\mathbf{H}) \cap \ker(\mathbf{W}) = \{\mathbf{0}\}$ and $\mathbf{M}^2(\mathbf{x}) \succeq \epsilon_M \text{Id}$. Then, $\mathcal{T}(\cdot, \mathbf{y}): \mathbb{R}^d \rightarrow B_r(\mathbf{0})$ maps into a ball around $\mathbf{0}$ with radius $r = \|\mathbf{H}\mathbf{y}\|_2 / \lambda_\epsilon$. If $\mathbf{M}^2: B_r(\mathbf{0}) \rightarrow [\epsilon, 1]^{N_{\text{out}}HW}$ is Lipschitz continuous with constant L , then $\mathcal{T}(\cdot, \mathbf{y})$ admits a fixed point and*

$$\|\mathcal{T}(\mathbf{x}_1, \mathbf{y}) - \mathcal{T}(\mathbf{x}_2, \mathbf{y})\|_2 \leq \frac{L \|\mathbf{H}\mathbf{y}\|_2}{\lambda_\epsilon^2} \|\mathbf{x}_2 - \mathbf{x}_1\|_2. \quad (16)$$

The Lipschitz estimate (16) is very conservative and $\mathcal{T}(\cdot, \mathbf{y})$ appears to often be even a local contraction. If $\mathcal{T}(\cdot, \mathbf{y})$ is contractive for every $\mathbf{y} \in \mathbb{R}^M$, we get the following result.

Theorem 4.4. *Assume $\ker(\mathbf{H}) \cap \ker(\mathbf{W}) = \{\mathbf{0}\}$ and $\mathbf{M}^2(\mathbf{x}) \succeq \epsilon_M \text{Id}$. If $\mathcal{T}(\cdot, \mathbf{y}): \mathbb{R}^d \rightarrow \mathbb{R}^d$ is contractive, i.e., if $\|\mathcal{T}(\mathbf{x}_1, \mathbf{y}) - \mathcal{T}(\mathbf{x}_2, \mathbf{y})\|_2 \leq q \|\mathbf{x}_1 - \mathbf{x}_2\|_2$ with $q < 1$, then the iterations (6) converge to a unique fixed point $\hat{\mathbf{x}}$ and*

$$\|\mathbf{x}_k - \hat{\mathbf{x}}\|_2 \leq q^{k-1} \|\mathbf{x}_1 - \mathbf{x}_0\|_2. \quad (17)$$

In particular, we have exponential convergence of (6). Moreover, if $\hat{\mathbf{x}} = \mathcal{T}(\hat{\mathbf{x}}, \mathbf{y}_1)$ and $\hat{\mathbf{z}} = \mathcal{T}(\hat{\mathbf{z}}, \mathbf{y}_2)$, then it holds

$$\|\hat{\mathbf{x}} - \hat{\mathbf{z}}\| \leq \frac{1}{1-q} \frac{\|\mathbf{H}\|_2}{\lambda_\epsilon} \|\mathbf{y}_1 - \mathbf{y}_2\|_2. \quad (18)$$

5. Experiments

We compare our method to state-of-the-art PnP approaches and learned regularizers on denoising, super-resolution, and MRI reconstruction. In Appendix C.1, we provide experimental results for grayscale deblurring.

5.1. Grayscale and Color Denoising

We corrupt ground-truth images by adding white Gaussian noise with standard deviation $\sigma_n \in \{5, 15, 25\}$. For various methods, we provide the respective average peak signal-to-noise ratios (PSNR) over the images of the BSD68 set and the center-cropped (256x256) images of CBS68 set in Table 1. Since some approaches are implemented for grayscale images only, parts of the table are left blank. First, we include (C)BM3D [7] as a widely regarded classic baseline. We also evaluate against WCRR [12], an unadaptive field-of-expert model of the form (2) that employs weakly convex potentials ψ_c . We also include its data-adaptive counterpart SARR [32, 31]. Regarding the refinement perspective (3), we include SAFI [35], which utilizes $\psi_c = \ell_1$ instead of ℓ_2 . Lastly, we include the deep learning-based approaches DnCNN [52], DRUNet [54] and ProxDRUNet [16]. The latter trades performance for improved theoretical guarantees compared to DRUNet. DEAL outperforms existing spatially adaptive methods and closes the gap to DRUNet-based approaches while having 30 times fewer parameters. We provide qualitative results in Figure 3, where we also provide the structural similarity index metric (SSIM). In the

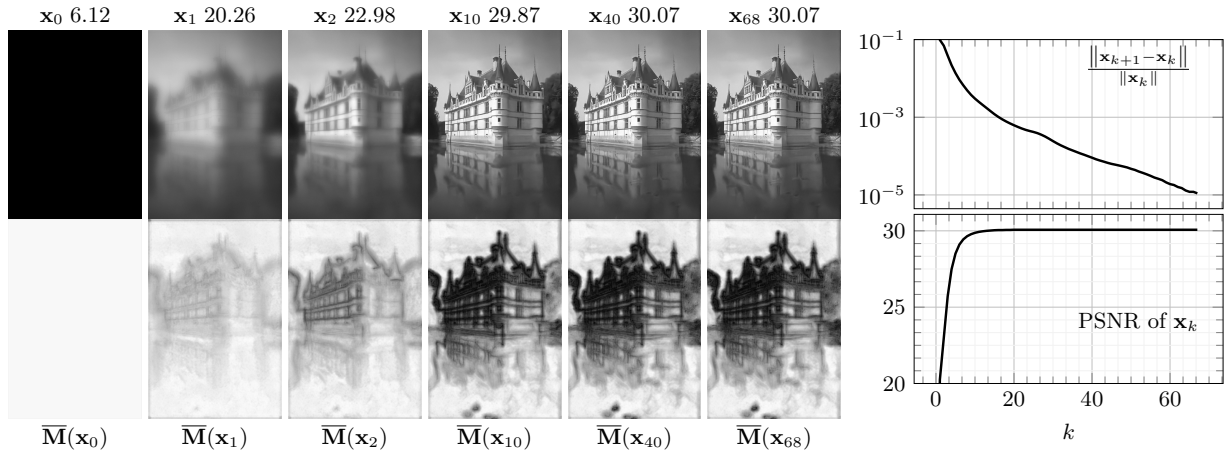


Figure 4: Solution path and channel-wise averages $\bar{\mathbf{M}}$ of the weights for DEAL iterations, exemplified with the *castle* image and $\sigma_n = 25$. On the right, we plot the residual values and PSNR over the number of outer iteration k .

Table 1: Denoising for the BSD68 and CBSD68 datasets.

σ_n	Gray			Color		
	5	15	25	5	15	25
BM3D	37.54	31.13	28.61	39.89	33.17	30.38
WCRR	37.65	31.20	28.68	—	—	—
SARR	37.80	31.61	29.13	—	—	—
SAFI	37.90	31.56	29.05	—	—	—
DEAL (Ours)	37.85	31.61	29.16	40.04	<u>33.61</u>	<u>30.93</u>
Prox-DRUNet	<u>37.97</u>	31.70	29.18	<u>40.12</u>	33.60	30.82
DNCNN	—	<u>31.72</u>	<u>29.23</u>	39.80	33.55	30.87
DRUNet	38.09	31.94	29.48	40.19	33.85	31.21

Table 2: PSNR values for color-image superresolution.

	$s=2$			$s=3$		
	2.55	7.65	12.75	2.55	7.65	12.75
DEAL (Ours)	27.99	<u>26.58</u>	25.75	26.20	<u>25.27</u>	24.59
Prox-DRUNet	27.88	26.61	<u>25.79</u>	<u>26.13</u>	25.29	24.67
IRCNN	26.97	25.86	25.45	25.60	25.72	24.38
DPIR	27.79	<u>26.58</u>	25.83	26.05	<u>25.27</u>	<u>24.66</u>

magnified part, we can see that DEAL does better than the DRUNet-based approaches in retaining structures such as the *tip* of the tower. In Figure 4, we provide the solution path associated to (6), the averages of the masks $\bar{\mathbf{M}}(\mathbf{x}_k)$, and two convergence plots. Specifically, the weights $\bar{\mathbf{M}}$ extract the image structure, leading to lower regularization cost at edges.

Table 3: PSNR values for the MRI experiment.

	4-fold single coil		8-fold multi-coil	
	PD	PDFS	PD	PDFS
Zero-fill ($\mathbf{H}^\top \mathbf{y}$)	27.40	29.68	23.80	27.19
TV	32.44	32.67	32.77	33.38
WCRR	35.78	34.63	35.57	35.16
SARR	36.25	34.77	35.98	35.26
SAFI	36.43	34.92	36.06	35.36
DEAL (Ours)	36.59	<u>34.92</u>	36.21	<u>35.32</u>
Prox-DRUNet	36.20	35.05	35.82	35.12
PnP-DnCNN	35.24	34.63	35.11	35.14

5.2. Color Super-resolution

Here, the forward \mathbf{H} involves two steps: the blurring of the image through the convolution with a known kernel; followed by a downsampling with $s \in \{2, 3\}$ that reduces the number of measurements by a factor of s^2 . As further degradation, AGWN of standard deviation σ_n is added to the image. We deploy the four Gaussian blur kernels from [54] with standard deviations (0.7, 1.2, 1.6 and 2.0), and report the average over these for the center-cropped images of CBSD68 in Table 2. There, DPIR [54] represents the state-of-the-art PnP approach; and IRCNN [53] is a competing PnP approach. The hyperparameters of DEAL are set to $\sigma = 15$ and $\lambda \in \{0.28, 2.5, 5.5\}$ for the three given noise levels $\sigma_n \in \{2.55, 7.65, 12.75\}$, respectively. We outperform existing methods on the lower noise levels and achieve comparable performance for the other cases. In Figure 5, we provide a visual comparison.

5.3. MRI Reconstruction

Now, we deploy DEAL for magnetic resonance imaging (MRI) tasks. Specifically, we tackle the single- and 15-coil MRI setups detailed by Goujon et al.

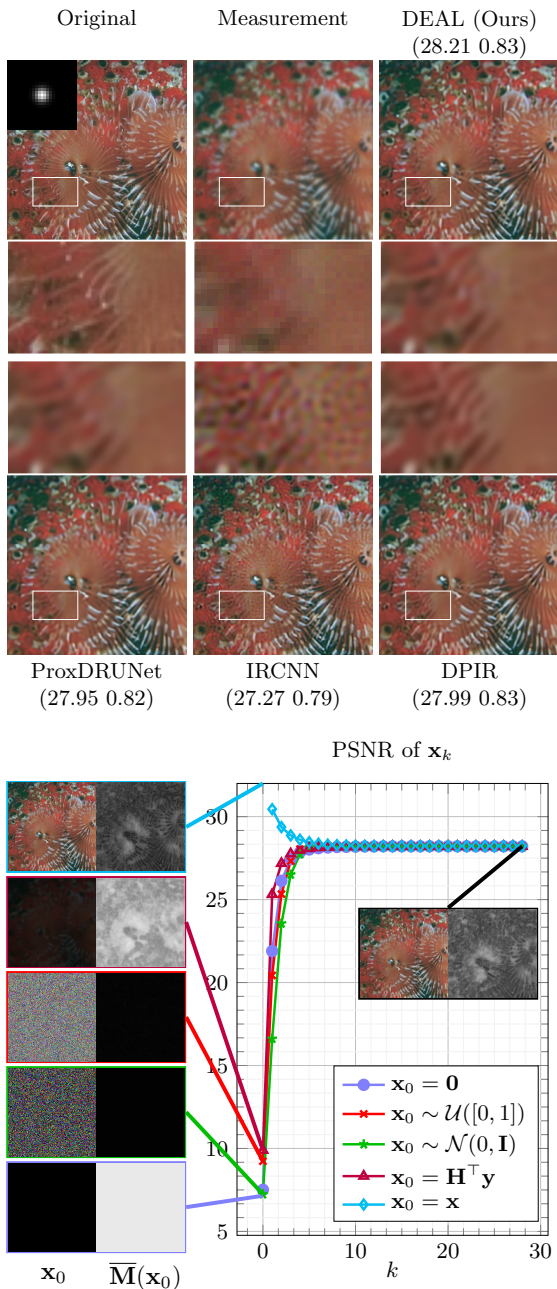


Figure 5: Superresolution task with rate $s = 2$ and $\sigma_n = 2.55$. The bottom image illustrates the dependence on initialization.

Table 4: Computation time (seconds) for the MRI experiment.

	4-fold single coil		8-fold multi-coil	
	PD	PDFS	PD	PDFS
WCRR	12	20	9	8
SAFI	436	470	388	326
DEAL (Ours)	<u>14</u>	<u>17</u>	<u>22</u>	<u>18</u>
Prox-DRUNet	113	38	170	105

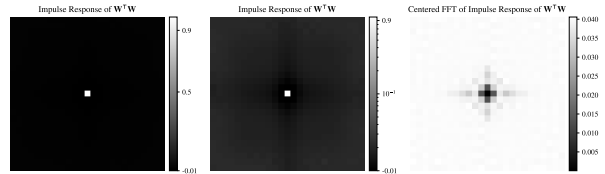


Figure 6: Different visualizations of $\mathbf{W}^\top \mathbf{W}$. Only one eigenvalue is numerically zero. The middle plot is on a logarithmic scale.

[11]. There, the ground-truth consists of knee images from the fastMRI dataset [19], both with fat suppression (PDFS) and without fat suppression (PD). The forward \mathbf{H} involves k -fold subsampling in the Fourier domain and corruption by additive white Gaussian noise with $\sigma_n = 0.002$. For each of the four evaluation tasks, we use ten images to tune the hyperparameters of all methods. In Table 3, we report the PSNR values on centered (320×320) patches of the remaining fifty test images. We compare against the popular TV regularization, the convex CRR regularizer [11], its weakly convex extension WCRR, and the Prox-DRUNet. All methods are *universal* in that they can be deployed without task-specific training. In Table 4, we report the computation times for several methods on a Tesla V100-SXM2-32GB GPU. We are significantly faster than the iterative refinement approach SAFI and get close to the (non-adaptive) WCRR baseline. Qualitative results are given in Figure 10 of Appendix C.2.

6. Interpretability and Robustness

In Figures 5 and 11, we demonstrate empirically that DEAL is not tied to a specific number K_{out} of iterations (6). In particular, doing more updates does not degrade the performance, unlike many PnP methods such as DPIR. The convergence to a fixed point (see Theorem 4.3) occurs for all experiments. In particular, both the relative error and the PSNR converge. To demonstrate the robustness regarding initialization, we instantiate the superresolution task. As we see in Figure 5, DEAL converges (in about 10 steps) to the same reconstruction independent of the initialization. This is in accordance with Theorem 4.4. The relative errors for this task are given in Figure 12 of Appendix C.3, underlining once more the empirical convergence.

We present visualizations for all parts of our architecture in Appendix D. Remarkably, we find mostly finite differences and their higher-order counterparts at various scales within \mathbf{W} (see Figure 13 in the appendix). These filters extract the salient features of the input. The impulse response of $\mathbf{W}^\top \mathbf{W}$ and its Fourier transform are given in Figure 6. Empirically, we observe that $\ker(\mathbf{W}) = \text{span}(\mathbf{1}_d)$. This is a practical certification for the condition of Proposition

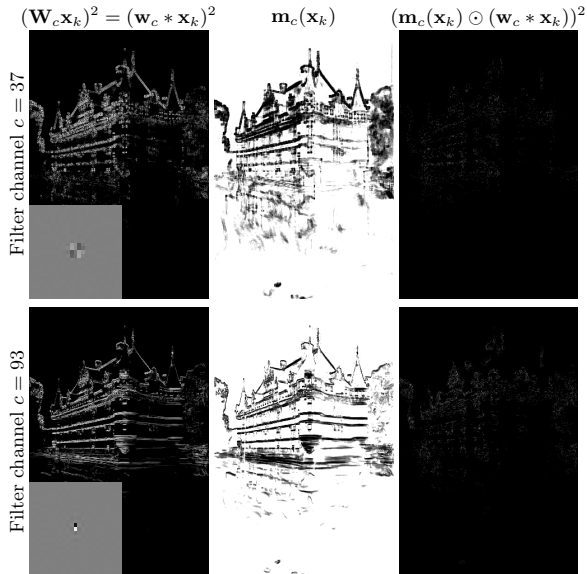


Figure 7: From left to right: two example filters \mathbf{W}_c along with $(\mathbf{W}_c \mathbf{x}_k)^2$; the corresponding masks $\mathbf{m}_c(\mathbf{x}_k)$; and adapted squared response. The mask eliminates the structure of the image in the squared responses. Hence, DEAL preserves salient structures.

4.1.

Next, we present two interpretations of the learned attention mechanism. For simplicity, we focus on the castle denoising example from Figure 3 with the final solution \mathbf{x}_k . In Figure 7, we illustrate two learned filters within \mathbf{W}_c and the response $\mathbf{W}_c \mathbf{x}_k$ to these filters. The associated weights (masks) $\mathbf{m}_c(\mathbf{x}_k)$ are well adapted to the structural features captured by these filters. In effect, the mask suppresses the image structures in the final squared responses $(\mathbf{m}_c(\mathbf{x}_k) \odot (\mathbf{w}_c * \mathbf{x}_k))^2$, leading to a reduced regularization cost in (4). This is desirable as the image structure should not contribute to the regularization cost.

Next, we describe our second interpretation. Since we are in the denoising setting ($\mathbf{H} = \mathbf{I}$), we have $\mathbf{x}_k = \mathbf{A}_{k-1}^{-1} \mathbf{y}$ with $\mathbf{A}_{k-1} = \mathbf{I} + \lambda \mathbf{W}^\top \mathbf{M}(\mathbf{x}_{k-1})^2 \mathbf{W}$. Therefore, the mapping from the measurements \mathbf{y} to the solution \mathbf{x}_k is simply a linear transformation. More precisely, the n -th component of \mathbf{x}_k is a weighted average of the measurements \mathbf{y} with the weight given by the n -th row of \mathbf{A}_{k-1}^{-1} . To extract this row, we apply \mathbf{A}_{k-1}^{-1} to the n -th unit vector \mathbf{e}_n . Since \mathbf{x} and \mathbf{y} are vectorized images, we reshape the rows accordingly for Figure 8. There, we see that $\mathbf{A}_{k-1}^{-1} \mathbf{e}_n$ aligns well with the structure of the neighborhood around the n -th pixel of the image. This indicates that spatial information is encoded into \mathbf{A}_{k-1} during the refinements. In the first and second rows, the averaging occurs in the vertical and horizontal directions, respectively. In contrast, the image of the third row exhibits little structure, and DEAL averages over a larger region, with an emphasis on the center pixel. Thus, at equilibrium, DEAL acts

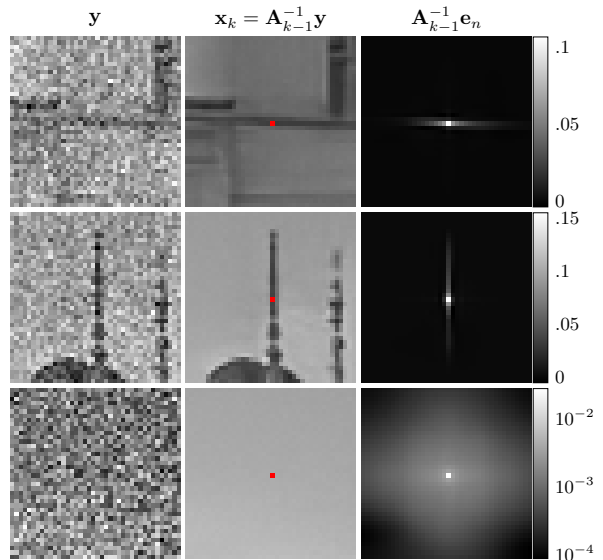


Figure 8: The reconstruction \mathbf{x}_k (middle) at the n -th entry (in red) is the weighted average of the data \mathbf{y} (left) with the weights (right) that come from the matrix \mathbf{A}_{k-1}^{-1} , i.e., $\mathbf{x}_k[n] = \langle \mathbf{A}_{k-1}^{-1} \mathbf{e}_n, \mathbf{y} \rangle$. Top to bottom: three different regions of the castle image.

as an adaptive averaging mechanism, intelligently averaging the noisy measurements \mathbf{y} , with weights that emerge from our iterative refinements.

7. Conclusion

We have presented deep attentive least squares (DEAL) for image reconstruction. DEAL builds upon classic signal processing ideas, which we blended with recent advances in deep learning, particularly, infinite-depth networks. It consists of two parts: (i) an iterative refinement of intermediate reconstructions based on a least-square-type problem; and (ii) a recurrent attention mechanism that adapts the problem spatially. We achieved competitive performance on different tasks while being able to provide interpretability, universality, and theoretical guarantees.

So far, we only trained DEAL on the denoising task. If sufficient data is available, it appears possible to fine tune all components of DEAL to further improve its performance. Moreover, DEAL is designed for the ℓ_2 data fidelity, and devising extensions for other data-fidelity terms is an interesting direction of future work.

Acknowledgements

M.P. and M.U. acknowledge support from the European Research Council (ERC Project FunLearn) under Grant 101020573, in part by the Swiss National Science Foundation, Grant 200020_219356. S.N. and E.K. acknowledge support from the DFG within the SPP2298 under project number 543939932. E.K. ac-

knowledges support from the Austrian Science Fund (FWF) project number 10.55776/COE12.

References

- [1] Cem Anil, Ashwini Pokle, Kaiqu Liang, Johannes Treutlein, Yuhuai Wu, Shaojie Bai, J Zico Kolter, and Roger Baker Grosse. Path independent equilibrium models can better exploit test-time computation. In *Advances in Neural Information Processing Systems*, volume 35, pages 7796–7809, 2022.
- [2] Shaojie Bai, J. Zico Kolter, and Vladlen Koltun. Deep equilibrium models. In *Advances in Neural Information Processing Systems*, volume 32, 2019.
- [3] Pakshal Bohra, Joaquim Campos, Harshit Gupta, Shayan Aziznejad, and Michael Unser. Learning activation functions in deep (spline) neural networks. *IEEE Open Journal of Signal Processing*, 1:295–309, 2020. doi: 10.1109/OJSP.2020.3039379.
- [4] Kristian Bredies and Dirk Lorenz. *Mathematical Image Processing. Applied and Numerical Harmonic Analysis*. Springer International Publishing, 2018. doi: 10.1007/978-3-030-01458-2.
- [5] R. H. Chan, S. Setzer, and G. Steidl. Inpainting by Flexible Haar-Wavelet Shrinkage. *SIAM Journal on Imaging Sciences*, 1(3):273–293, 2008. doi: 10.1137/070711499.
- [6] Yunjin Chen, Rene Ranftl, and Thomas Pock. Insights into analysis operator learning: From patch-based sparse models to higher order MRFs. *IEEE Transactions on Image Processing*, 23(3):1060–72, 2014. doi: 10.1109/TIP.2014.2299065.
- [7] Kostadin Dabov, Alessandro Foi, Vladimir Katkovnik, and Karen Egiazarian. Image denoising by sparse 3-D transform-domain collaborative filtering. *IEEE Transactions on Image Processing*, 16(8):2080–2095, 2007. doi: 10.1109/TIP.2007.901238.
- [8] Mohammad Zalbagi Darestani, Vishwesh Nath, Wenqi Li, Yufan He, Holger R. Roth, Ziyue Xu, Daguang Xu, Reinhard Heckel, and Can Zhao. IR-FRestormer: Iterative refinement with fourier-based restormer for accelerated mri reconstruction. In *IEEE/CVF Winter Conference on Applications of Computer Vision*, pages 7640–7649, 2024.
- [9] Stanislas Ducotterd, Alexis Goujon, Pakshal Bohra, Dimitris Perdios, Sebastian Neumayer, and Michael Unser. Improving Lipschitz-constrained neural networks by learning activation functions. *Journal of Machine Learning Research*, 25:1–30, 2024.
- [10] Alexander Effland, Erich Kobler, Karl Kunisch, and Thomas Pock. Variational networks: An optimal control approach to early stopping variational methods for image restoration. *Journal of Mathematical Imaging and Vision*, 62(3):396–416, 2020.
- [11] Alexis Goujon, Sebastian Neumayer, Pakshal Bohra, Stanislas Ducotterd, and Michael Unser. A neural-network-based convex regularizer for inverse problems. *IEEE Transactions on Computational Imaging*, 9:781–795, 2023. doi: 10.1109/TCI.2023.3306100.
- [12] Alexis Goujon, Sebastian Neumayer, and Michael Unser. Learning weakly convex regularizers for convergent image-reconstruction algorithms. *SIAM Journal on Imaging Sciences*, 17(1):91–115, 2024.
- [13] Markus Grasmair and Frank Lenzen. Anisotropic Total Variation Filtering. *Applied Mathematics & Optimization*, 62(3):323–339, 2010. doi: 10.1007/s00245-010-9105-x.
- [14] Johannes Hertrich, Sebastian Neumayer, and Gabriele Steidl. Convolutional proximal neural networks and Plug-and-Play algorithms. *Linear Algebra and its Applications*, 631:203–234, 2021.
- [15] Michael Hintermüller, Konstantinos Papafitsoros, and Carlos N. Rautenberg. Analytical aspects of spatially adapted total variation regularisation. *Journal of Mathematical Analysis and Applications*, 454(2):891–935, 2017. doi: 10.1016/j.jmaa.2017.05.025.
- [16] Samuel Hurault, Arthur Leclaire, and Nicolas Papadakis. Proximal denoiser for convergent Plug-and-Play optimization with nonconvex regularization. In *International Conference on Machine Learning*, volume 162, pages 9483–9505, 2022.
- [17] Samuel Hurault, Arthur Leclaire, and Nicolas Papadakis. Gradient step denoiser for convergent Plug-and-Play. In *International Conference on Learning Representations*, 2022.
- [18] Diederik P. Kingma and Jimmy Ba. Adam: A method for stochastic optimization. In *International Conference on Learning Representations*, 2015.
- [19] Florian Knoll, Jure Zbontar, Anuroop Sriram, Matthew J. Muckley, Mary Bruno, Aaron Defazio, Marc Parente, Krzysztof J. Geras,

- Joe Katsnelson, Hersh Chandarana, Zizhao Zhang, Michal Drozdalv, Adriana Romero, Michael Rabbat, Pascal Vincent, James Pinkerton, Duo Wang, Nafissa Yakubova, Erich Owens, C. Lawrence Zitnick, Michael P. Recht, Daniel K. Sodickson, and Yvonne W. Lui. fastMRI: A publicly available raw k-space and DICOM dataset of knee images for accelerated MR image reconstruction using machine learning. *Radiology: Artificial Intelligence*, 2(1):e190007, 2020.
- [20] Erich Kobler, Alexander Effland, Karl Kunisch, and Thomas Pock. Total Deep Variation: A Stable Regularization Method for Inverse Problems. *IEEE Transactions on Pattern Analysis and Machine Intelligence*, 44(12):9163–9180, 2022. doi: 10.1109/TPAMI.2021.3124086.
- [21] Andreas Kofler, Fabian Altekrieger, Fatima Antarou Ba, Christoph Kolbitsch, Evangelos Papoutsellis, David Schote, Clemens Sirotenko, Felix Frederik Zimmermann, and Kostas Papafitsoros. Learning regularization parameter-maps for variational image reconstruction using deep neural networks and algorithm unrolling. *SIAM Journal on Imaging Sciences*, 16(4):2202–2246, 2023. doi: 10.1137/23M1552486.
- [22] Jakob Kruse, Carsten Rother, and Uwe Schmidt. Learning to push the limits of efficient FFT-based image deconvolution. In *IEEE International Conference on Computer Vision*, pages 4586–4594, 2017.
- [23] Stamatios Lefkimmiatis and Iaroslav Sergeevich Koshelev. Learning sparse and low-rank priors for image recovery via iterative reweighted least squares minimization. In *International Conference on Learning Representations*, 2023.
- [24] F. Lenzen, J. Lellmann, F. Becker, and C. Schnörr. Solving quasi-variational inequalities for image restoration with adaptive constraint sets. *SIAM Journal on Imaging Sciences*, 7(4):2139–2174, 2014. doi: 10.1137/130938347.
- [25] Frank Lenzen and Johannes Berger. Solution-driven adaptive total variation regularization. In *International Conference on Scale Space and Variational Methods in Computer Vision*, pages 203–215, 2015.
- [26] Anat Levin, Yair Weiss, Fredo Durand, and William T Freeman. Understanding and evaluating blind deconvolution algorithms. In *IEEE Conference on Computer Vision and Pattern Recognition*, pages 1964–1971. IEEE, 2009.
- [27] Housen Li, Johannes Schwab, Stephan Anholzer, and Markus Haltmeier. NETT: Solving inverse problems with deep neural networks. *Inverse Problems*, 36(6):065005, 2020. doi: 10.1088/1361-6420/ab6d57.
- [28] Sebastian Lunz, Ozan Öktem, and Carola-Bibiane Schönlieb. Adversarial regularizers in inverse problems. In *Advances in Neural Information Processing Systems*, volume 31, 2018.
- [29] Stephane Mallat. *A Wavelet Tour of Signal Processing*. Academic Press, 1999.
- [30] Michael T. McCann and Michael Unser. Biomedical image reconstruction: From the foundations to deep neural networks. *Foundations and Trends® in Signal Processing*, 13(3):283–359, 2019. doi: 10.1561/2000000101.
- [31] Sebastian Neumayer and Fabian Altekrieger. Stability of data-dependent ridge-regularization for inverse problems. *arXiv:2406.12289*, 2024.
- [32] Sebastian Neumayer, Mehrsa Pourya, Alexis Goujon, and Michael Unser. Boosting weakly convex ridge regularizers with spatial adaptivity. In *NeurIPS Workshop on Deep Learning and Inverse Problems*, 2023.
- [33] Jiahao Pang and Gene Cheung. Graph laplacian regularization for image denoising: Analysis in the continuous domain. *IEEE Transactions on Image Processing*, 26(4):1770–1785, 2017. doi: 10.1109/TIP.2017.2651400.
- [34] Jean-Christophe Pesquet, Audrey Repetti, Matthieu Terris, and Yves Wiaux. Learning Maximally Monotone Operators for Image Recovery. *SIAM Journal on Imaging Sciences*, 14(3):1206–1237, 2021. doi: 10.1137/20M1387961.
- [35] Mehrsa Pourya, Sebastian Neumayer, and Michael Unser. Iteratively refined image reconstruction with learned attentive regularizers. *Numerical Functional Analysis and Optimization*, 45(7-9):411–440, 2024. doi: 10.1080/01630563.2024.2384849.
- [36] Monica Pragliola, Luca Calatroni, Alessandro Lanza, and Fiorella Sgallari. On and beyond total variation regularization in imaging: The role of space variance. *SIAM Review*, 65(3):601–685, 2023. doi: 10.1137/21M1410683.
- [37] Jean Prost, Antoine Houdard, Andrés Almansa, and Nicolas Papadakis. Learning Local Regularization for Variational Image Restoration. In *International Conference on Scale Space and Variational Methods in Computer Vision*, pages 358–370, Cham, 2021. doi: 10.1007/978-3-030-75549-2_29.
- [38] Edward T Reehorst and Philip Schniter. Regularization by denoising: Clarifications and new interpretations. *IEEE Transactions on Computational Imaging*, 5(1):52–67, 2018.

- [39] Yaniv Romano, Michael Elad, and Peyman Milanfar. The little engine that could: Regularization by denoising (RED). *SIAM Journal on Imaging Sciences*, 10(4):1804–1844, 2017.
- [40] Stefan Roth and Michael J Black. Fields of experts. *International Journal of Computer Vision*, 82(2):205–229, 2009.
- [41] Leonid I Rudin, Stanley Osher, and Emad Fatemi. Nonlinear total variation based noise removal algorithms. *Physica D: Nonlinear Phenomena*, 60(1-4):259–268, 1992.
- [42] Chitwan Saharia, Jonathan Ho, William Chan, Tim Salimans, David J. Fleet, and Mohammad Norouzi. Image super-resolution via iterative refinement. *IEEE Transactions on Pattern Analysis and Machine Intelligence*, 45(4):4713–4726, 2023. doi: 10.1109/TPAMI.2022.3204461.
- [43] Zachary Teed and Jia Deng. RAFT-3D: Scene Flow using Rigid-Motion Embeddings. In *IEEE/CVF Conference on Computer Vision and Pattern Recognition*, pages 8371–8380. IEEE, 2021. doi: 10.1109/CVPR46437.2021.00827.
- [44] Diego Valsesia, Giulia Fracastoro, and Enrico Magli. Deep graph-convolutional image denoising. *IEEE Transactions on Image Processing*, 29:8226–8237, 2020. doi: 10.1109/TIP.2020.3013166.
- [45] Cao Van Chung, Juan Carlos De los Reyes, and Carola Schönlieb. Learning optimal spatially-dependent regularization parameters in total variation image denoising. *Inverse Problems*, 33(7):074005, 2017. doi: 10.1088/1361-6420/33/7/074005.
- [46] Singanallur V Venkatakrishnan, Charles A Bouman, and Brendt Wohlberg. Plug-and-Play priors for model based reconstruction. In *IEEE Global Conference on Signal and Information Processing*, pages 945–948, 2013.
- [47] Joachim Weickert. *Anisotropic Diffusion in Image Processing*, volume 1. Teubner Stuttgart, 1998.
- [48] Martin Zach, Florian Knoll, and Thomas Pock. Stable deep MRI reconstruction using generative priors. *IEEE Transactions on Medical Imaging*, 42(12):3817–3832, 2023. doi: 10.1109/TMI.2023.3311345.
- [49] Martin Zach, Erich Kobler, Antonin Chambolle, and Thomas Pock. Product of Gaussian Mixture Diffusion Models. *Journal of Mathematical Imaging and Vision*, 66(4):504–528, 2024. doi: 10.1007/s10851-024-01180-3.
- [50] Gengsheng Lawrence Zeng. Image reconstruction—a tutorial. *Computerized medical imaging and graphics*, 25(2):97–103, 2001.
- [51] Jin Zeng, Jiahao Pang, Wenxiu Sun, and Gene Cheung. Deep graph laplacian regularization for robust denoising of real images. In *IEEE/CVF Conference on Computer Vision and Pattern Recognition Workshops*, pages 1759–1768, 2019. doi: 10.1109/CVPRW.2019.00226.
- [52] Kai Zhang, Wangmeng Zuo, Yunjin Chen, Deyu Meng, and Lei Zhang. Beyond a gaussian denoiser: Residual learning of deep cnn for image denoising. *IEEE Transactions on Image Processing*, 26(7):3142–3155, 2017. doi: 10.1109/TIP.2017.2662206.
- [53] Kai Zhang, Wangmeng Zuo, Shuhang Gu, and Lei Zhang. Learning deep CNN denoiser prior for image restoration. In *IEEE Conference on Computer Vision and Pattern Recognition*, pages 3929–3938, 2017.
- [54] Kai Zhang, Yawei Li, Wangmeng Zuo, Lei Zhang, Luc Van Gool, and Radu Timofte. Plug-and-play image restoration with deep denoiser prior. *IEEE Transactions on Pattern Analysis and Machine Intelligence*, 44(10):6360–6376, 2022. doi: 10.1109/TPAMI.2021.3088914.
- [55] Daniel Zoran and Yair Weiss. From learning models of natural image patches to whole image restoration. In *IEEE International Conference on Computer Vision*, pages 479–486, 2011.

A. DEAL Hyperparameters and Ablation Studies

For the linear splines φ_1 , φ_2 and φ_3 appearing in \mathbf{M} we fix $r = 3$, $N_n = 31$. Moreover, we initialize φ_1 and φ_2 as the absolute value $|\cdot|$ and φ_3 as $e^{-(\cdot)^2}$, motivated by classical anisotropic diffusion [47]. Each s_c in (11) has 14 knots in the range $[-1, 51]$. They are initialized as the constant function 3. We choose $\sigma = \sigma_n$ in \mathbf{M} , where σ_n is the standard deviation of a sample's noise. We set $\lambda = \kappa(\sigma_n)$ with a learnable spline κ defined using 52 knots in $[-1, 51]$ initialized as the identity. The denoisers are strongly tied, particularly, \mathbf{W} and \mathbf{M} must work across various settings.

We used $N_c = 128$ number of filters. We observed that if we reduce N_c to 64 or 32, we degrade the performance for denoising on $\sigma = 25$ by around 0.1 and 0.15, respectively. We also observed that going beyond the filter size (9×9) in the Multi-Conv block does not improve the performance. The proposed constraints and initializations for the learning of the non-linearities stem from the learning of such parts without any constraints and with zero initialization.

B. Proofs

B.1. Proof of Proposition 4.1

Proof. Assume that there exists $\mathbf{x} \in \mathbb{R}^d \setminus \{\mathbf{0}\} \in \ker(\mathbf{A}_k)$, namely with $\mathbf{x}^\top \mathbf{A}_k \mathbf{x} = \mathbf{0}$. By definition of \mathbf{A}_k , this implies $\mathbf{x}^\top \mathbf{H}^\top \mathbf{H} \mathbf{x} = \mathbf{0}$ and $\mathbf{x}^\top \mathbf{W}^\top \mathbf{M}^2(\mathbf{x}_k) \mathbf{W} \mathbf{x} = \mathbf{0}$. Hence, we get $\mathbf{x} \in \ker(\mathbf{H})$ and $\mathbf{x} \in \ker(\mathbf{M}(\mathbf{x}_k) \mathbf{W})$, which is a contradiction. For $\mathbf{M}^2(\mathbf{x}_k) \succeq \epsilon_M \text{Id}$, we estimate $\mathbf{A}_k \succeq \mathbf{H}^\top \mathbf{H} + \epsilon_M \mathbf{W}^\top \mathbf{W}$ and the uniqueness as in the first part. \square

B.2. Proof of Lemma 4.2

Proof. Let $\hat{\mathbf{x}} = \mathcal{T}(\mathbf{x}, \mathbf{y}_1)$ and $\hat{\mathbf{z}} = \mathcal{T}(\mathbf{x}, \mathbf{y}_2)$, namely $\mathbf{A}_x \hat{\mathbf{x}} = \mathbf{H}^\top \mathbf{y}_1$ and $\mathbf{A}_x \hat{\mathbf{z}} = \mathbf{H}^\top \mathbf{y}_2$. This implies that $\mathbf{A}_x(\hat{\mathbf{x}} - \hat{\mathbf{z}}) = \mathbf{H}^\top(\mathbf{y}_1 - \mathbf{y}_2)$ and we estimate

$$\|\hat{\mathbf{x}} - \hat{\mathbf{z}}\|_2 \leq \frac{\|\mathbf{H}\|_2}{\lambda_\epsilon} \|\mathbf{y}_1 - \mathbf{y}_2\|_2. \quad (19)$$

B.3. Proof of Theorem 4.3

Proof. First, we investigate the range of $\mathcal{T}(\cdot, \mathbf{y})$. By definition of $\mathcal{T}(\cdot, \mathbf{y})$, it holds for any $\mathbf{x} \in \mathbb{R}^d$ that

$$\|\mathcal{T}(\mathbf{x}, \mathbf{y})\|_2 = \|\mathbf{A}_k^{-1} \mathbf{H}^\top \mathbf{y}\|_2 \leq \frac{\|\mathbf{H} \mathbf{y}\|_2}{\lambda_\epsilon}. \quad (20)$$

For the second part, we want to apply Brouwer's fixed-point theorem. To this end, we must prove that $\mathcal{T}(\cdot, \mathbf{y})$ is continuous. Let $\mathbf{x}_1, \mathbf{x}_2 \in \mathbb{R}^d$, $\hat{\mathbf{x}}_1 = \mathcal{T}(\mathbf{x}_1, \mathbf{y})$ and $\hat{\mathbf{x}}_2 = \mathcal{T}(\mathbf{x}_2, \mathbf{y})$. Then, it holds

$$\begin{aligned} \mathbf{A}_1 \hat{\mathbf{x}}_1 - \mathbf{A}_2 \hat{\mathbf{x}}_2 &= \mathbf{0} \\ \mathbf{A}_1 \hat{\mathbf{x}}_1 - \mathbf{A}_1 \hat{\mathbf{x}}_2 &= \mathbf{A}_2 \hat{\mathbf{x}}_2 - \mathbf{A}_1 \hat{\mathbf{x}}_2 \\ \hat{\mathbf{x}}_1 - \hat{\mathbf{x}}_2 &= \mathbf{A}_1^{-1} (\mathbf{A}_2 - \mathbf{A}_1) \hat{\mathbf{x}}_2. \end{aligned} \quad (21)$$

Incorporating (20) and the normalization $\|\mathbf{W}\|_2 = 1$, we further infer

$$\begin{aligned} \|\hat{\mathbf{x}}_1 - \hat{\mathbf{x}}_2\|_2 &\leq \|\mathbf{A}_1^{-1}\|_2 \|\mathbf{W}\|_2^2 \|\mathbf{M}^2(\mathbf{x}_2) - \mathbf{M}^2(\mathbf{x}_1)\|_2 \|\hat{\mathbf{x}}_2\|_2 \\ &\leq \frac{L \|\mathbf{H} \mathbf{y}\|_2}{\lambda_\epsilon^2} \|\mathbf{x}_2 - \mathbf{x}_1\|_2. \end{aligned} \quad (22)$$

Hence, $\mathcal{T}(\cdot, \mathbf{y})$ is Lipschitz continuous and a fixed-point exists. \square

B.4. Proof of Theorem 4.4

Proof. Due to the Banach fixed point theorem, the exponential convergence rate (17) holds. To estimate the difference of $\hat{\mathbf{x}} = \mathcal{T}(\hat{\mathbf{x}}, \mathbf{y}_1)$ and $\hat{\mathbf{z}} = \mathcal{T}(\hat{\mathbf{z}}, \mathbf{y}_2)$, we use the contractivity of $\mathcal{T}(\cdot, \mathbf{y}_1)$ and Lemma 4.2 to get

$$\begin{aligned} \|\hat{\mathbf{x}} - \hat{\mathbf{y}}\|_2 &= \|\mathcal{T}(\hat{\mathbf{x}}, \mathbf{y}_1) - \mathcal{T}(\hat{\mathbf{z}}, \mathbf{y}_2)\|_2 \leq \|\mathcal{T}(\hat{\mathbf{x}}, \mathbf{y}_1) - \mathcal{T}(\hat{\mathbf{z}}, \mathbf{y}_1)\|_2 + \|\mathcal{T}(\hat{\mathbf{z}}, \mathbf{y}_1) - \mathcal{T}(\hat{\mathbf{z}}, \mathbf{y}_2)\|_2 \\ &\leq q \|\hat{\mathbf{x}} - \hat{\mathbf{z}}\|_2 + \frac{\|\mathbf{H}\|_2}{\lambda_\epsilon} \|\mathbf{y}_1 - \mathbf{y}_2\|_2. \end{aligned} \quad (23)$$

Table 5: PSNR values for grayscale deblurring.

	$\sigma = 2.55$						$\sigma = 7.65$					
	17x17			27x27			17x17			27x27		
	C.man	House	Monarch	C.man	House	Monarch	C.man	House	Monarch	C.man	House	Monarch
EPLL	29.18	32.33	27.32	27.85	28.13	22.92	24.82	28.50	23.03	24.31	26.02	20.86
DEAL (Ours)	<u>31.72</u>	<u>35.20</u>	<u>32.77</u>	<u>31.64</u>	<u>35.03</u>	<u>32.48</u>	<u>27.89</u>	<u>32.24</u>	<u>28.26</u>	<u>27.79</u>	<u>32.11</u>	<u>28.15</u>
FDN	29.09	29.75	29.13	28.78	29.29	28.60	26.18	28.01	25.86	26.13	27.41	25.39
IRCNN	31.69	35.04	32.71	31.56	34.73	32.42	27.70	31.94	28.23	27.58	31.55	27.99
DPIR	32.05	35.82	33.38	31.97	35.52	32.99	28.17	32.79	28.48	27.99	32.87	28.27

From this, we readily infer (18), namely

$$\|\hat{\mathbf{x}} - \hat{\mathbf{y}}\|_2 \leq \frac{\|\mathbf{H}\|_2}{(1-q)\lambda_\epsilon} \|\mathbf{y}_1 - \mathbf{y}_2\|_2. \quad (24)$$

□

C. Additional Numerical Results

C.1. Grayscale Deblurring

Here, we evaluate the DEAL approach for a grayscale deblurring task. We use the same setup as DPIR for this experiment [54]. This includes two blur kernels of sizes 17×17 and 27×27 from [26] and additive Gaussian noise with $\sigma_n = 2.55$ and $\sigma_n = 7.65$. In Table 5, we report the PSNR of the reconstructions for the Set3 images, namely Cameraman, House, and Monarch. We set the model noise level $\sigma = 15$ and $\lambda \in \{0.5, 2.5\}$ for the two given AWGN noise levels σ_n , respectively. We also compare with model-based EPLL [55] and the learning approach FDN that is specific to deblurring [22]. We observe that we are consistently the second-best method on this task after DPIR. We provide a visual comparison with DPIR in Figure 9.

C.2. Visualizations for MRI Reconstruction

We provide visual reconstruction examples obtained with different methods from Table 3 in Figure 10. We also provide the solution path and the convergence plots for DEAL in Figure 11.

C.3. Convergence Plot for Superresolution

In Figure 12, we represent the convergence plot for the superresolution task on the setup of Figure 5. Again, we empirically observe the convergence of our method.

D. Visualization of Model Components

Now, we inspect the components of our learned grayscale model. In Figure 13, we depict the impulse response of \mathbf{W} , i.e., the block’s equivalent convolution kernels (a.k.a filters). The convolutions of \mathbf{W}_{mask} have similar structure as we see in Figure 14. In addition, we depict the learned splines in Figure 15. For ϕ_c^σ , we visualize three different noise levels $\sigma \in \{5, 15, 25\}$ and channels $c \in \{44, 93, 99\}$. The three visualized channels correspond to vertical edge filters of various scales, see Figure 13. They resemble threshold functions that set high responses to zero. This results in less regularization in the regions that have high responses to the filters that are often activated by the image structures. This is a desirable behavior as the structure of the image should not contribute to the regularization cost. Additionally, the widths of the last spline ϕ_c^σ are increasing for all channels with respect to the noise level σ . Thus, more regularization is performed for higher noise levels. Moreover, we show the channel-wise average of the masks for the noisy and the denoised *castle* image in Figure 16. The masks remove the undesirable contribution of the image to the filter responses $\mathbf{W}\mathbf{x}$ of the regularizer. This results in lower penalization of the edges and yields sharper solutions.

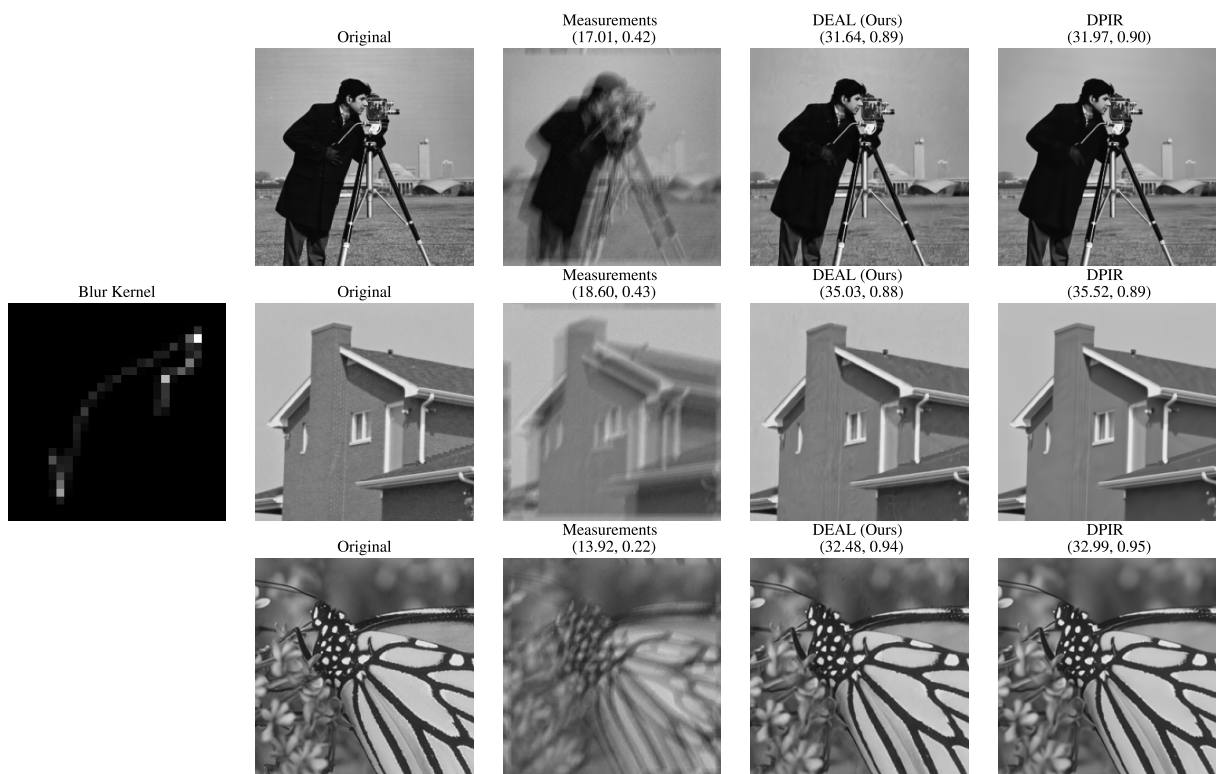


Figure 9: Deblurring results for the given blur kernel and noise level $\sigma_n = 2.55$.

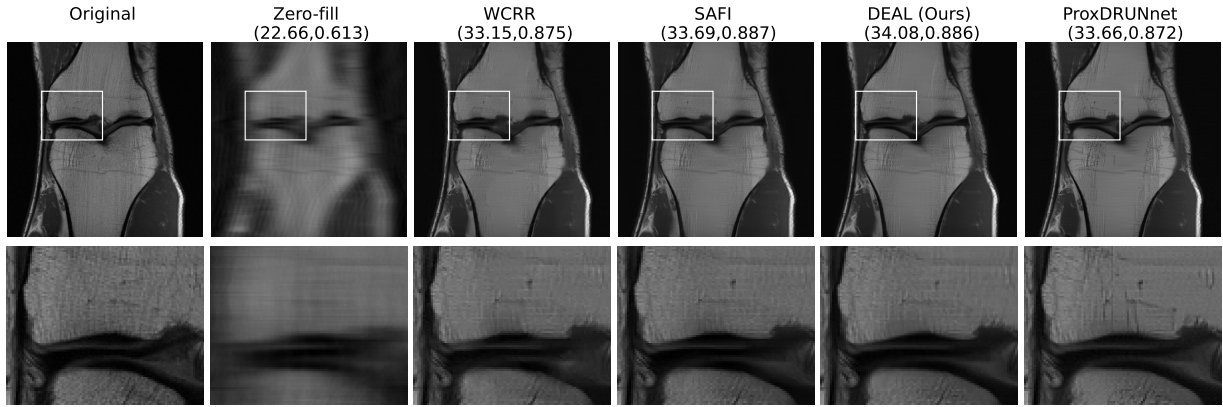


Figure 10: Comparison of different methods for 8-fold multi-coil MRI reconstruction for a PD image of the knee.

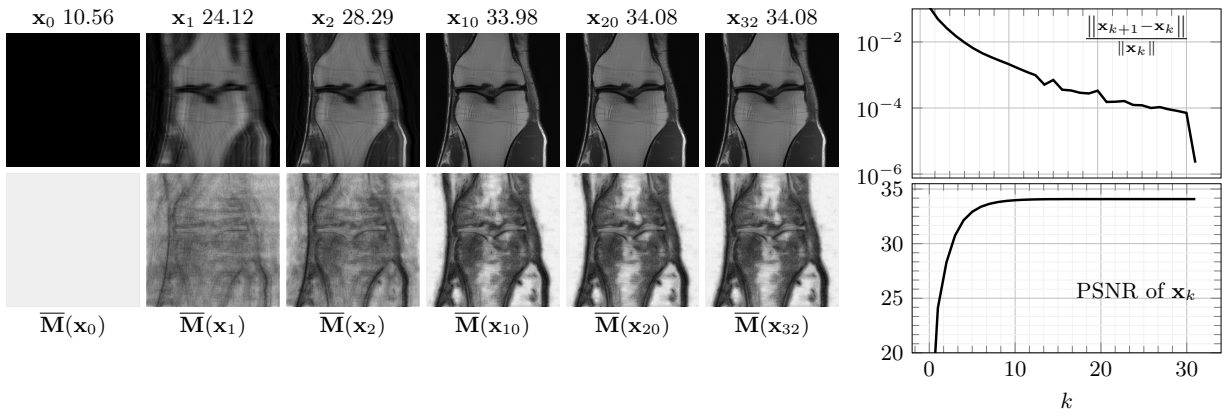


Figure 11: Solution and mask path for the 8-fold multi-coil MRI reconstruction for a PD image of knee.

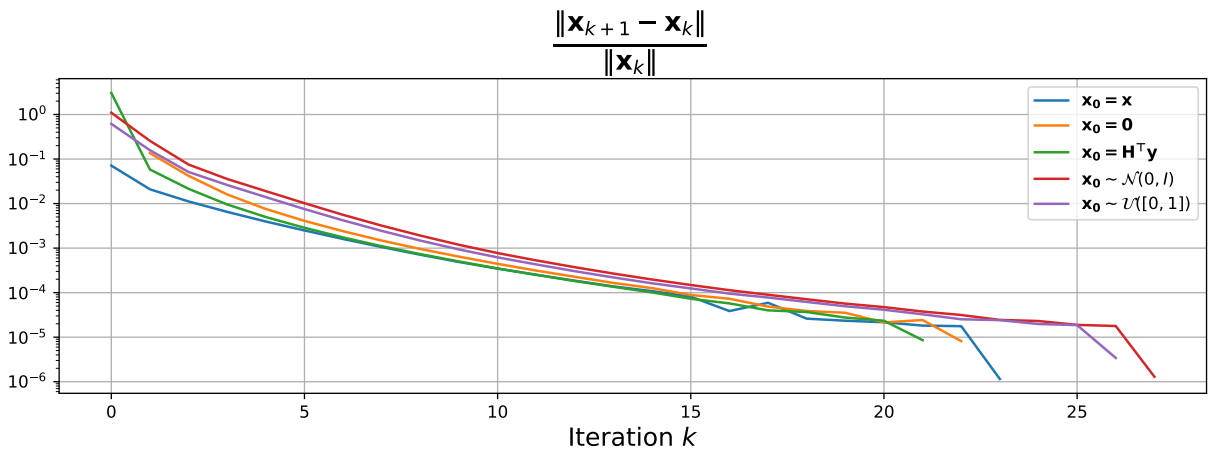


Figure 12: Convergence plot for the super resolution task with $s = 2$ and noise level $\sigma_n = 2.55$ for different initializations.

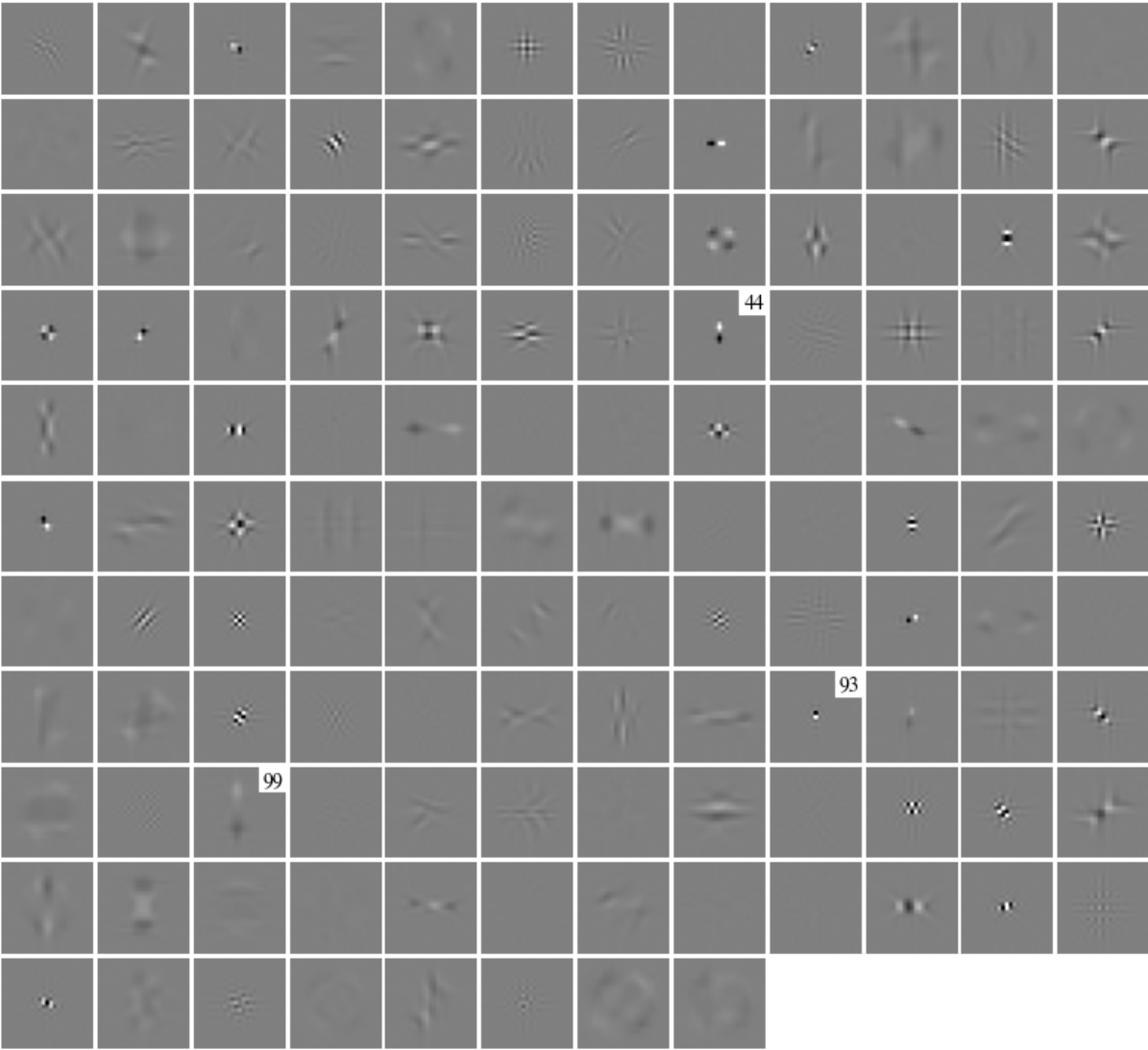


Figure 13: Effective convolution kernels for the Multi-Conv block \mathbf{W} in the grayscale model. All plots use the same range, where gray corresponds to zero. Brighter filters are more important.

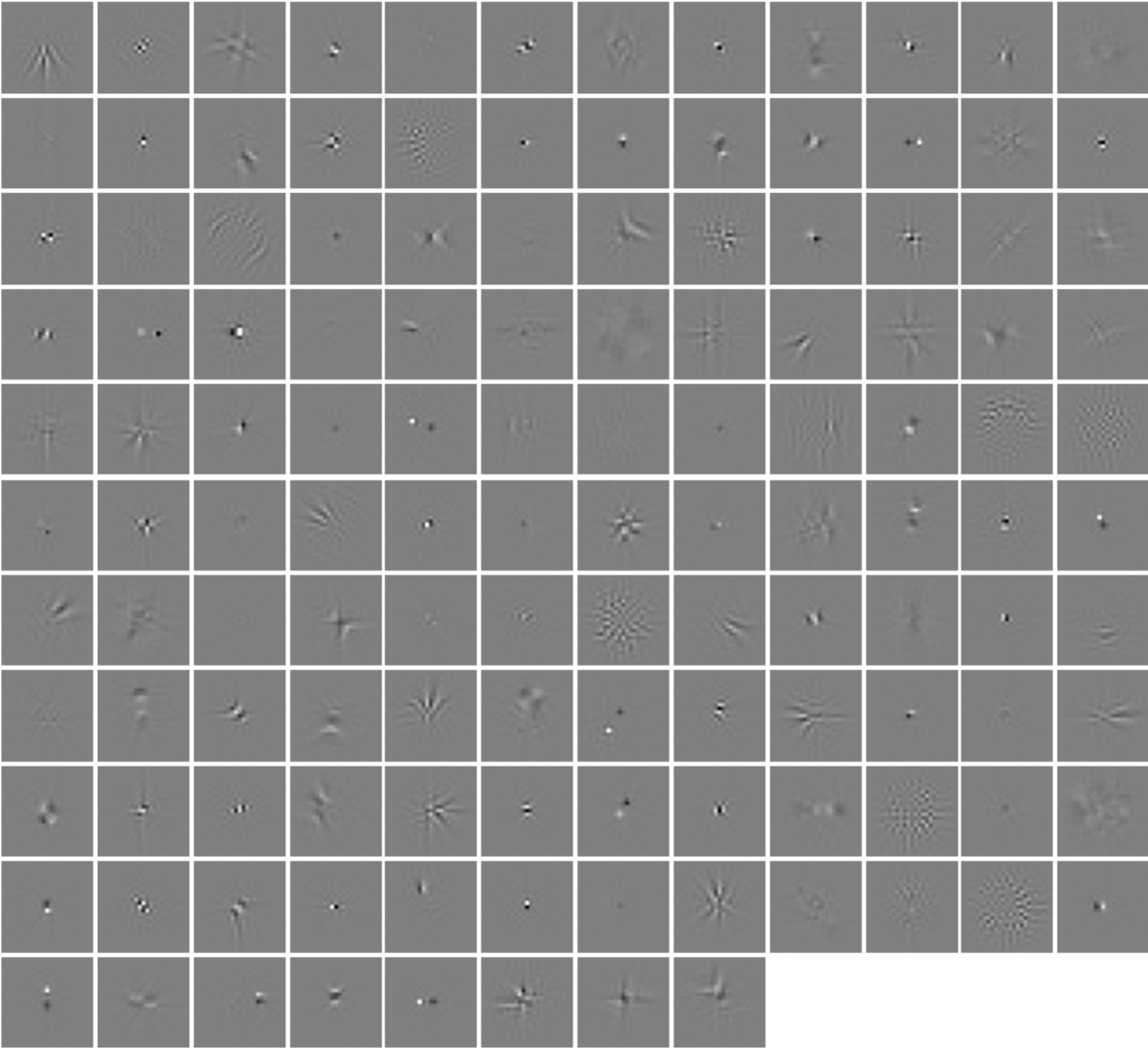


Figure 14: Effective convolution kernels for the Multi-Conv block \mathbf{W}_{mask} in the grayscale model. All plots use the same range, where gray corresponds to zero. Brighter filters are more important.

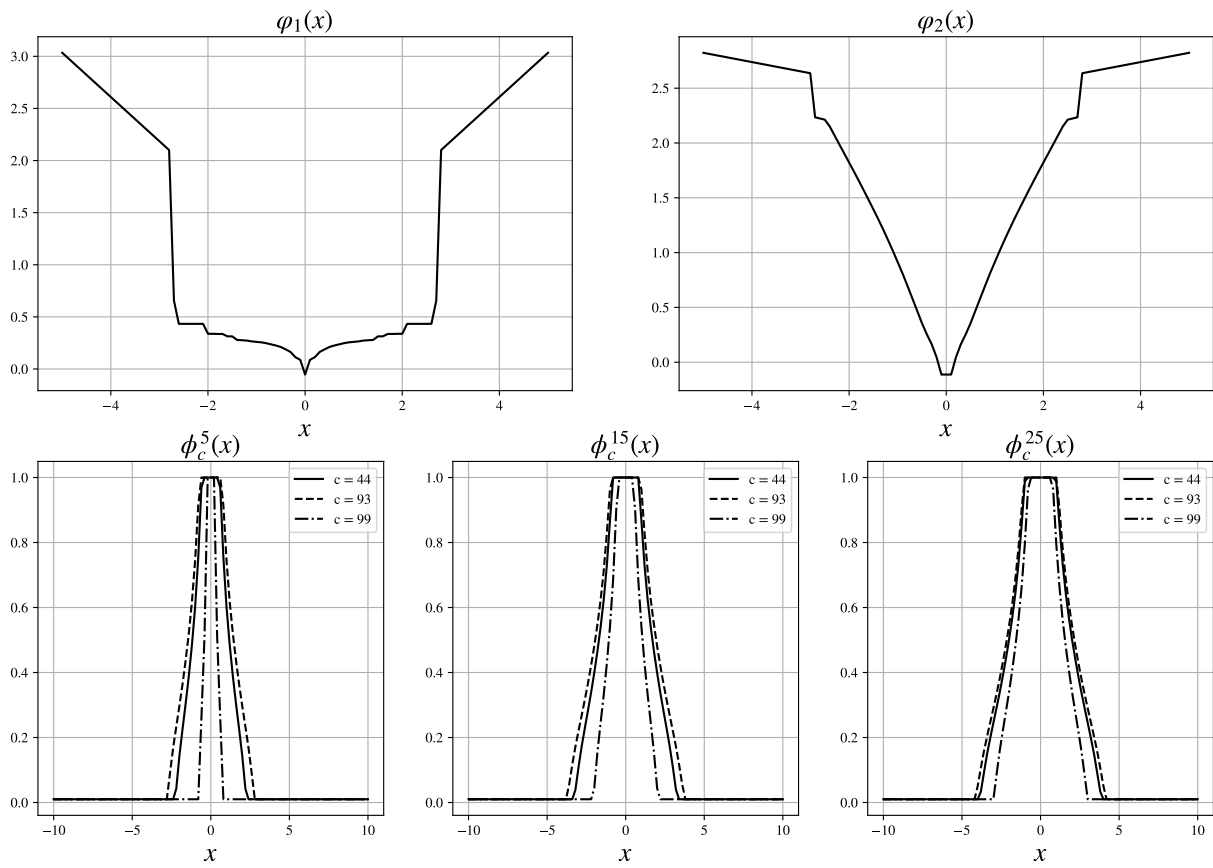


Figure 15: Learned splines in the mask generation network \mathbf{M} (Figure 2) for grayscale model.

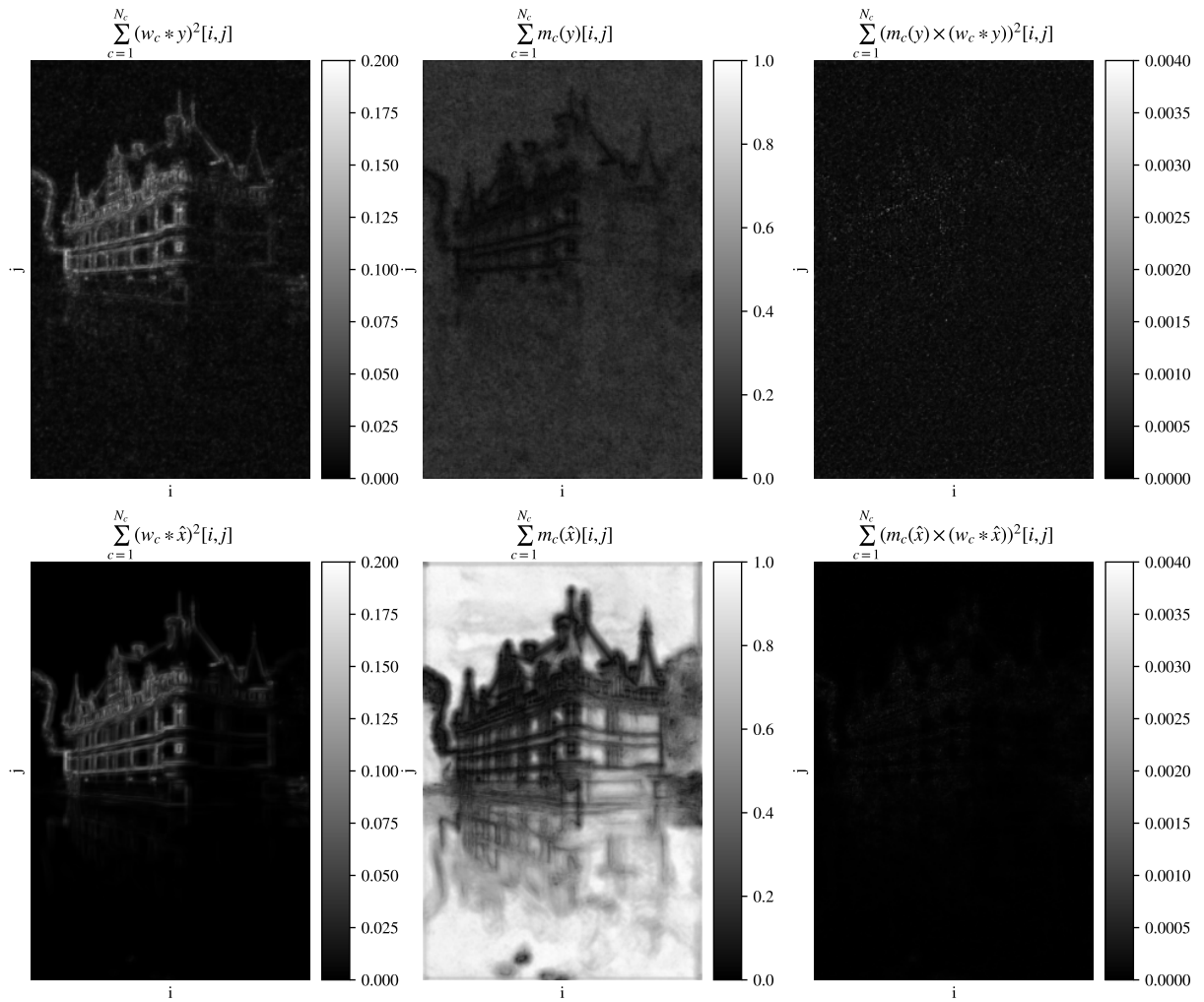


Figure 16: From left to right: a channel-wise average of (i) the squared response to the noisy image (top) and the solution of the castle denoising problem (bottom); (ii) the masks computed on the noisy image (top) and the solution (bottom), (iii) corresponding adapted responses.